electronic reprint

Structures of the SEp22 dodecamer, a Dps-like protein from *Salmonella enterica* subsp. *enterica* serovar Enteritidis

Takanori Miyamoto, Yasuko Asahina, Shohei Miyazaki, Hidetoshi Shimizu, Umeharu Ohto, Shuji Noguchi and Yoshinori Satow

Crystallography Journals Online is available from journals.iucr.org

Structures of the SEp22 dodecamer, a Dps-like protein from *Salmonella enterica* subsp. *enterica* serovar Enteritidis

Takanori Miyamoto, Yasuko Asahina, Shohei Miyazaki, Hidetoshi Shimizu, Umeharu Ohto, Shuji Noguchi and Yoshinori Satow*

Graduate School of Pharmaceutical Sciences, The University of Tokyo, Japan

Correspondence e-mail:
fwkozo@mail.ecc.u-tokyo.ac.jp

The crystal structure of SEp22, a DNA-binding protein from starved cells from *Salmonella enterica* subsp. *enterica* serovar Enteritidis, has been determined in two forms: the native state at 1.25 Å resolution and an iron-soaked form at 1.30 Å resolution. The SEp22 protomers form a dodecameric shell with 23 symmetry and a single iron ion per protomer was found at the ferroxidase centre in the iron-soaked form. Along the threefold axes of the 23 symmetry, hydrophilic Asp channels that consist of Asp146 were found. Iron ions may flow into the cavity of the dodecameric shell through the Asp channels.

1. Introduction

Salmonella enterica subsp. *enterica* serovar Enteritidis (SE) is an anaerobic Gram-negative bacterium that causes salmonellosis in humans *via* contaminated foods such as hen eggs (Nataro *et al.*, 2007). SEp22 is a protein produced by SE which consists of 166 amino acids and belongs to the DNA-binding-protein-from-starved-cells-like (Dps-like) protein family (Terai *et al.*, 2005). Dps-like proteins are dodecameric; they were initially discovered in *Escherichia coli* (Almiron *et al.*, 1992) and were subsequently found in bacteria and archaea. Currently, over 1000 Dps-like proteins have been identified and approximately 97% of them are from bacteria, with the remaining Dps-like proteins being from archaea (Haikarainen & Papageorgiou, 2010). Dps-like proteins are able to incorporate Fe^{2+} ions inside their dodecameric shell and the incorporated Fe^{2+} ions are oxidized to Fe^{3+} ions at the ferroxidase centre (FOC) located within the dodecamer (Haikarainen & Papageorgiou, 2010). Subsequently, the Fe^{3+} ions are presumed to be mineralized and stored in the form of hydrous ferric oxide (Zhao *et al.*, 2002). Dps-like proteins are considered to protect DNA from oxidative damage caused by reactive oxygen species (ROS) such as hydroxyl radicals. Hydroxyl radicals are generated from H_2O_2 and Fe^{2+} *via* the Fenton reaction (Imlay, 2003). Dps-like proteins prevent ROS production *via* the Fenton reaction by sequestering Fe^{2+} ions. SEp22 is expressed from the late logarithmic phase to the stable phase in the proliferation of SE (Terai *et al.*, 2005). SE infections are eliminated by ROS produced by human macrophages. The expression of SEp22 has been reported to be induced by H_2O_2 and SE expressing SEp22 has been reported to have higher resistance to ROS (Terai *et al.*, 2006). These observations indicate that the anti-ROS activity of SEp22 is crucial for the survival of an SE infection in humans.

Some Dps-like proteins, such as *E. coli* Dps, are able to bind to double-stranded DNA through a flexible N-terminal tail containing one Arg and three Lys residues that appear to interact with the negatively charged sugar-phosphate backbone of DNA (Grant *et al.*, 1998; Roy *et al.*, 2004, 2007; Stillman *et al.*, 2005). The SEp22 protomer has three lysine residues (Lys5, Lys8 and Lys10) that are located in the N-terminal tail (Terai *et al.*, 2005). Consequently, the tail is expected to bind to DNA.

In this paper, we report the crystal structures of the SEp22 dodecamer in native and iron-soaked forms at 1.25 and 1.30 Å resolution, respectively. The structures reveal the details of the FOC of SEp22 with bound iron ion and the channels through which the iron ions flow into the cavity of SEp22.
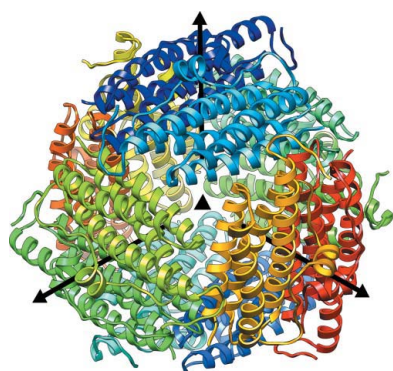
Table 1
Diffraction data and refinement statistics.

Values in parentheses are for the highest resolution shell.

	Native form	Iron-soaked form		
Crystal parameters				
Space group	$P2_12_12_1$	$P2_12_12_1$		
Unit-cell parameters (Å)	$a = 94.7$, $b = 98.4$, $c = 208.9$	$a = 94.5$, $b = 98.0$, $c = 208.4$		
Solvent content (%)	43.7	43.2		
Matthews coefficient ($\mathring{A}^3$ Da^{-1})	2.18	2.16		
No. of molecules in asymmetric unit	12	12		
Data collection				
X-ray wavelength (Å)	1.0000	1.0000	1.7400	1.7500
Resolution (Å)	50.0–1.25 (1.27–1.25)	50.0–1.30 (1.32–1.30)	30.0–2.00 (2.03–2.00)	30.0–2.00 (2.03–2.00)
$\langle I/\sigma(I)\rangle$	18.6 (3.43)	17.8 (2.40)	18.9 (5.60)	20.0 (6.24)
No. of observed reflections	2854420	1768328	424197	422495
No. of unique reflections	531051	428932	117185	116841
Completeness (%)	99.7 (99.9)	90.9 (89.6)	88.7 (83.4)	88.6 (83.2)
Multiplicity	5.4 (4.7)	4.1 (2.8)	3.6 (3.6)	3.6 (3.7)
R_{merge}†	0.075 (0.557)	0.061 (0.396)	0.054 (0.204)	0.042 (0.176)
Refinement				
No. of used reflections	504240	407378		
R_{work}‡/R_{free}§	0.164/0.205	0.153/0.173		
Mean temperature factor ($\mathring{A}^2$)	18.4	25.2		
Model composition				
No. of amino acids	1839	1835		
No. of non-H atoms	16660	16201		
No. of iron ions	0	12		
No. of magnesium ions	6	4		
No. of sulfate ions	6	6		
No. of water molecules	1644	1327		
Geometry				
R.m.s.d. bond lengths (Å)	0.022	0.022		
R.m.s.d. bond angles (°)	1.95	1.95		
Ramachandran plot, residues in				
Favoured region (%)	99.1	99.3		
Allowed region (%)	0.9	0.7		
Outlier region (%)	0.0	0.0		

† $R_{merge} = \sum_{hkl} \sum_i |I_i(hkl) - \langle I(hkl)\rangle| / \sum_{hkl} \sum_i I_i(hkl)$, where $I_i(hkl)$ is the intensity measured for a given reflection and $\langle I(hkl)\rangle$ is the average intensity for multiple measurements of this reflection. ‡ $R_{work} = \sum_{hkl} ||F_{obs}| - |F_{calc}|| / \sum_{hkl} |F_{obs}|$, where F_{obs} and F_{calc} are the observed and calculated structure-factor amplitudes, respectively, for 95% of the reflection data used in the refinement. § $R_{free} = \sum_{hkl} ||F_{obs}| - |F_{calc}|| / \sum_{hkl} |F_{obs}|$ for 5% of the reflection data that were excluded during refinement.

2. Materials and methods

2.1. Expression and purification of recombinant SEp22

The cDNA of the SEp22 gene tagged with *E. coli* maltose-binding protein (MBP) at its N-terminus was ligated into the plasmid vector pMAL-P2X (New England Biolabs, Ipswich, Massachusetts, USA) and *E. coli* JM109 competent cells were transformed with the plasmid. The cells were grown at 310 K in Luria–Bertini broth medium containing 100 µg ml^{-1} ampicillin and 1 µ*M* FeSO$_4$. The temperature was lowered to 298 K when the optical density at 600 nm reached 0.3 and isopropyl β-D-1-thiogalactopyranoside was added to a final concentration of 0.3 m*M* for the induction of the MBP-tagged recombinant SEp (MBP-SEp22). The cells were harvested after 8 h of culturing by centrifugation at 4000g and were lysed by resuspension in ice-cold 5 m*M* MgSO$_4$ solution. After centrifugation of the lysate, the supernatant solution was applied onto an affinity chromatography column packed with 30 ml amylose resin (New England Biolabs) at 277 K. After washing with eight column volumes of buffer *A* (200 m*M* NaCl, 20 m*M* Tris–HCl pH 7.4, 1 m*M* EDTA), MBP-SEp22 was eluted from the column with buffer *A* containing 10 m*M* maltose. The MBP tag of the eluted MBP-SEp22 was cleaved using 0.6 U bovine factor Xa (Merck, Whitehouse Station, New Jersey, USA) per milligram of MBP-SEp22. After 16 h incubation at 298 K, factor Xa was inactivated by adding 4-(2-aminoethyl)benzenesulfonyl fluoride to a final concentration of 1.0 m*M*. SEp22 without the tag was passed through a HiTrap Q HP anion-exchange column (GE Healthcare, Little Chalfont, England) pre-equilibrated with buffer *A* at 277 K and the flowthrough fractions were collected. The fractions that contained the target protein were pooled and the sample was

concentrated using an Amicon Ultra 30K concentrator (Millipore, Billerica, Massachusetts, USA). This material was loaded onto a 4.4 ml POROS 20 HS cation-exchange column (Applied Biosystems, Foster City, California, USA) pre-equilibrated with buffer *B* (240 m*M* NaCl, 25 m*M* MES pH 6.5, 1 m*M* EDTA) at room temperature. SEp22 was eluted with 50 ml buffer *B* containing a linear NaCl gradient from 240 to 620 m*M*. The eluted fraction was concentrated using an Amicon Ultra 30K concentrator and loaded onto a Superdex 200 HR 10/30 gel-filtration column (GE Healthcare) pre-equilibrated with a solution consisting of 75 m*M* MgSO$_4$, 10 m*M* sodium acetate buffer pH 5.3 at room temperature. The purified SEp22 was concentrated to 30 mg ml^{-1} using an Amicon Ultra 30K concentrator and used for crystallization. The protein concentration was determined from the absorbance at 280 nm and the calculated molar absorption coefficient of SEp22 (Gasteiger *et al.*, 2005). The purified SEp22 showed a single band on analysis by SDS–PAGE with Coomassie Brilliant Blue staining.

2.2. Crystallization

Crystallization was performed using the sitting-drop vapour-diffusion method. 0.5 µl purified SEp22 solution was mixed with 0.5 µl reservoir solution consisting of 100 m*M* sodium acetate buffer pH 5.3, 250–350 m*M* MgCl$_2$ and 28–29%(v/v) polyethylene glycol 400 and equilibrated against 100 µl reservoir solution at 293 K. SEp22 crystals appeared and grew to typical dimensions of 50 × 50 × 100 µm in 1–2 d. The reproducibility of the crystal was greatly improved by introducing microcrystals into the droplet using the streak-seeding method after 1–2 d of equilibration. To prepare iron-

soaked SEp22 crystals, the native SEp22 crystals were soaked for 5 d at 293 K in an iron-soaking solution consisting of 100 mM MES pH 6.0, 250 mM MgCl₂, 75 mM MgSO₄, 30%(v/v) polyethylene glycol 400, 100 mM ascorbic acid and 100 mM Fe(NH₄)₂(SO₄)₂. Soaking crystals in solutions with a higher Fe(NH₄)₂(SO₄)₂ concentration or for a longer period resulted in crystal cracking.

2.3. X-ray diffraction data collection and processing

Crystals were flash-frozen in a stream of N₂ at 95 K just prior to collection of the X-ray diffraction data. The concentrations of polyethylene glycol 400 in the droplet solution and iron-soaking solution were sufficiently high to prevent ice formation upon freezing. X-ray diffraction data collection was performed on beamlines BL-5A and NE-3A at the KEK Photon Factory (Tsukuba, Japan). The X-ray wavelength was set to 1.0000 Å. In order to identify the iron ions bound to SEp22 using anomalous dispersion signals from the iron

ions, two further data sets were collected from an iron-soaked crystal at wavelengths just above (1.7400 Å) and just below (1.7500 Å) the Fe K absorption edge (Bearden, 1967). The diffraction images were indexed and scaled using the HKL-2000 package (Otwinowski & Minor, 1997). The crystal parameters are summarized in Table 1.

2.4. Structure determination and refinement

The crystal structures were determined by the molecular replacement method using MOLREP as implemented in the CCP4 suite (Collaborative Computational Project, Number 4, 1994) with E. coli DPS (PDB entry 1dps; 95% amino-acid identity to SEp22; Grant et al., 1998) as the search model. Crystallographic refinements were performed with REFMAC5 (Murshudov et al., 1997) as implemented in the CCP4 suite. Noncrystallographic symmetry restraints were not included throughout the refinement. Model building and structure adjustments were performed using Coot (Emsley & Cowtan, 2004).
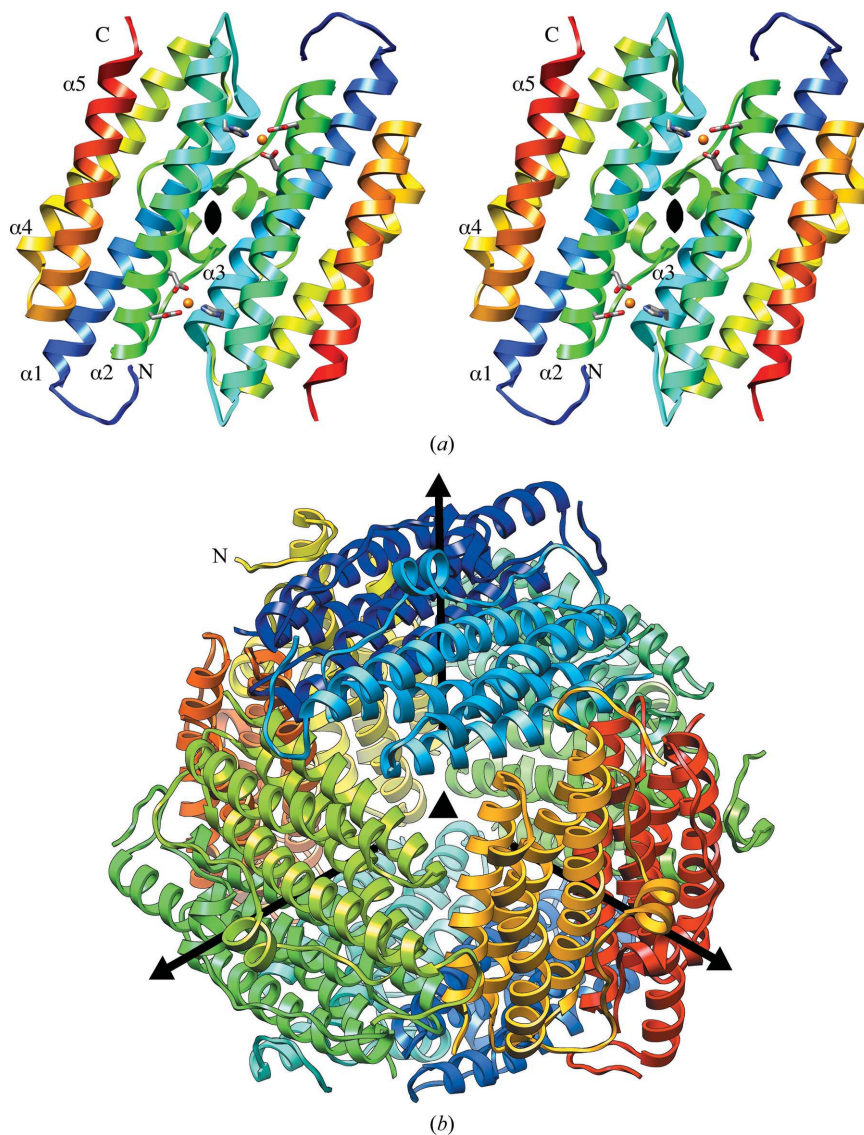
Figure 1
The dimeric and dodecameric structures of iron-soaked SEp22. (a) Stereoview of the iron-soaked dimeric protomers. The polypeptide chains are drawn as ribbon models. A twofold axis of the dimeric structure is shown as a black lens. The residues constituting the FOCs are shown as coloured stick models with carbon in grey, oxygen in red and nitrogen in blue. The iron ions are shown as orange spheres. The N- and C-termini and the α-helices in one protomer are labelled. (b) The structure of the iron-soaked dodecamer. The twofold and threefold symmetry axes of the dodecameric structure are shown as arrows (Poornam et al., 2009) and a black triangle, respectively. The N-terminus of one protomer is labelled. The bound metal ions and sulfate ions are omitted for clarity.
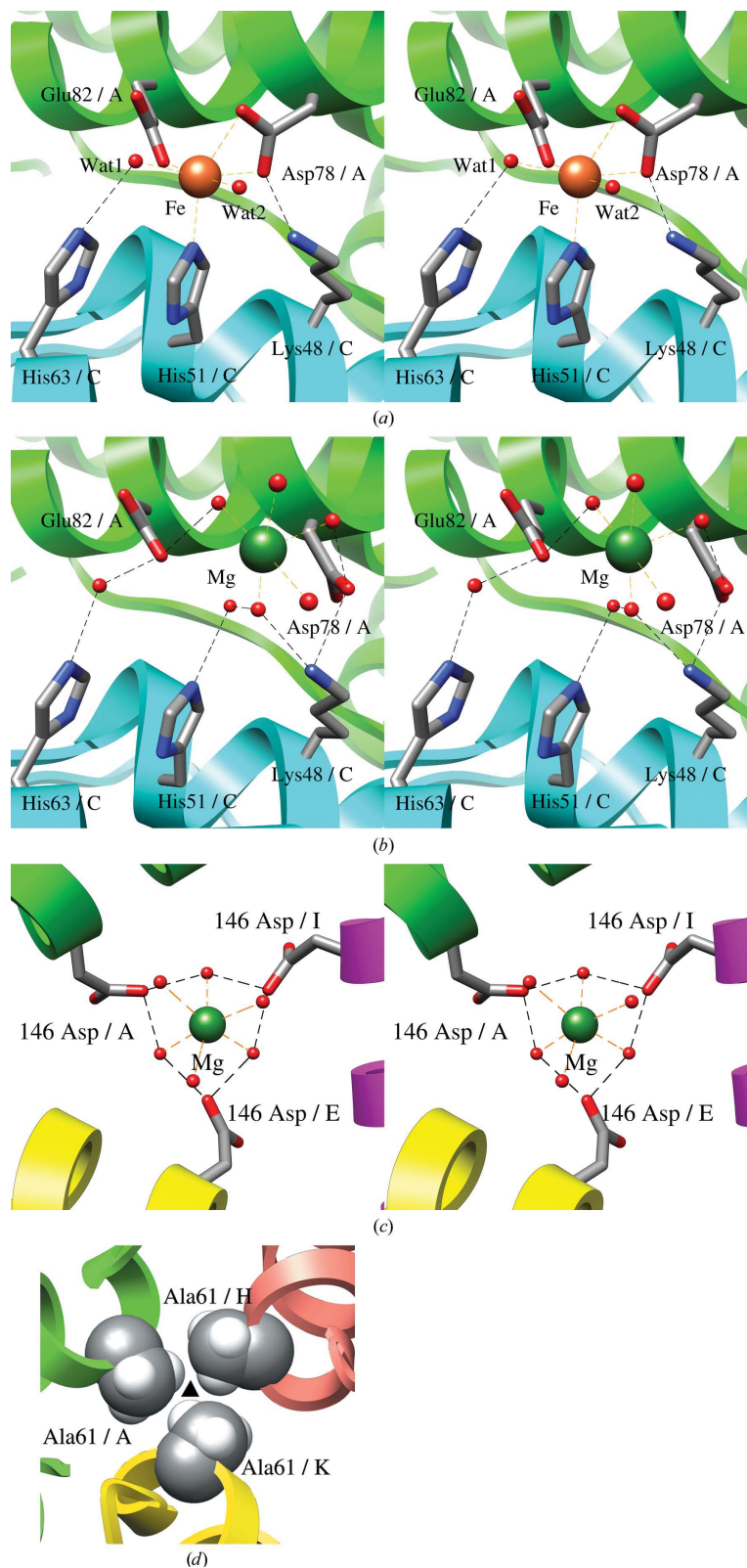
Figure 2
The structure of the FOCs, the Asp channel and the Ala weld. (*a*) Stereoview of the FOC between protomers *A* and *C* of the iron-soaked form. The polypeptide chains of protomers *A* and *C* are drawn as green and cyan ribbon models. The side chains of the residues at the FOCs are shown as stick models. The iron ion and water molecules are shown as orange and red spheres, respectively. The coordinate bonds between the iron ion and water molecules are shown as yellow dashed lines. Hydrogen bonds are shown as black dashed lines. (*b*) Stereoview of the FOC between protomers *A* and *C* in the native form. The magnesium ion is shown as a green sphere. The coordinate bonds between the magnesium ion and water molecules are shown as yellow dashed lines. (*c*) Stereoview of the Asp channel of the native form. The polypeptide chains of protomers *A*, *E* and *I* are drawn as green, yellow and magenta ribbon models, respectively. The Asp146 residues at the channel are shown as stick models. (*d*) Structure of the Ala weld. The polypeptide chains are drawn as ribbon models. C and H atoms of Ala61 are shown as white and grey CPK models, respectively. The threefold axis of the 23 symmetry is shown as a black triangle.

Table 2
Distances between the iron ion and liganding atoms.

Values are in Å. SD, standard deviation.

Protomer	Atom liganding to iron ion					
	Asp78 $O^{\delta1}$	Asp78 $O^{\delta2}$	Glu82 $O^{\varepsilon2}$	His51 $N^{\varepsilon2}$	Water 1	Water 2
A	2.33	2.31	1.95	2.18	1.93	2.21
B	2.28	2.31	1.95	2.18	2.00	2.22
C	2.31	2.30	1.96	2.19	1.85	2.22
D	2.33	2.31	1.97	2.16	1.96	2.15
E	2.32	2.33	1.97	2.17	1.95	2.17
F	2.31	2.33	1.94	2.20	1.92	2.18
G	2.34	2.32	1.98	2.18	1.90	2.18
H	2.33	2.33	1.97	2.15	1.93	2.26
I	2.32	2.36	1.95	2.18	1.83	2.17
J	2.27	2.34	1.97	2.21	1.88	2.12
K	2.32	2.35	1.93	2.18	1.81	2.24
L	2.34	2.38	1.95	2.16	1.93	2.22
Mean ± SD	2.32 ± 0.02	2.33 ± 0.02	1.96 ± 0.01	2.18 ± 0.02	1.91 ± 0.06	2.19 ± 0.04

Atomic displacement parameters (B factors) of the individual atoms were refined anisotropically after the resolution was extended to 1.3 Å and the R_{free} decreased to below 0.23. Iron ions were identified using a phased Bijvoet difference map. The occupancies of the iron ions were set to 1.0. Validation of the models was performed by *SFCHECK* (Vaguine *et al.*, 1999), *PROCHECK* (Laskowski *et al.*, 1993) and *RAMPAGE* (Lovell *et al.*, 2003) as implemented in the *CCP*4 suite. The superposition of the protomers and the calculation of the root-mean-square differences (r.m.s.d.s) between protomers were performed with *SuperPose* (Maiti *et al.*, 2004). The molecular images were drawn with *UCSF Chimera* (Pettersen *et al.*, 2004). The statistics of the X-ray diffraction data-collection and crystallographic refinement are summarized in Table 1.

The atomic coordinates and observed structure amplitudes of the native and iron-soaked forms have been deposited in the PDB under accession codes 3ak8 and 3ak9, respectively.

3. Results and discussion

3.1. Overall structure of SEp22

The crystal structures contain 12 protomers, *A–L*, per asymmetric unit. As the electron densities were ambiguous, probably owing to disorder, the following residues were not included in the model: Met1–Lys8 of protomer *F*, Met1–Ser12 of protomers *B–E* and *G–L* and Met1–Asn13 of protomer *A* for the native form; and Met1–Ser12 of protomers *A–C* and *E–L* and Met1–Asn13 of protomer *D* for the iron-soaked form. A protomer of SEp22 is composed of a four-α-helix bundle (helices α1, α2, α4 and α5) with an additional short helix (helix α3) oriented almost perpendicular to the bundle (Fig. 1*a*). 12 protomers form a spherical shell-like dodecamer with 23 symmetry (Fig. 1*b*). In the crystal, the SEp22 dodecamer forms crystal contacts with eight neighbouring dodecamers, giving a pseudo-body-centred packing which contrasts with the characteristic pseudo-hexagonal-sheet packing of the *E. coli* DPS crystal structure (Grant *et al.*, 1998). The approximate outer and inner diameters of the dodecamer are 85 and 45 Å, respectively. The approximate volume of the internal cavity is 5.2×10^4 Å^3 as calculated by *CASTp* (Dundas *et al.*, 2006). The positional r.m.s.d. of the C$^\alpha$ atoms between the native SEp22 and *E. coli* DPS dodecamers is 0.33 Å and that between the native and iron-soaked SEp22 dodecamers is 0.15 Å, indicating that the overall dodecameric structure of SEp22 does not change upon iron ion binding. The positional r.m.s.d.s of the C$^\alpha$ atoms among the native protomers, among the iron-soaked protomers and among both the native and iron-soaked protomers are 0.10, 0.09 and 0.09 Å, respec-

tively. These low r.m.s.d. values indicate that all the protomers in these crystal structures are essentially identical. However, small structural differences are observed in three regions of both forms: Asn13–Tyr16, Ser22–Lys27 and Ala139–Asp141. The maximum C$^\alpha$-atom displacement within these regions of superposed native SEp22 protomers is 1.39 Å at Asn13 (between protomers *F* and *K*), 0.81 Å at Ser24 (between protomers *B* and *D*) and 1.77 Å at Lys140 (between protomers *C* and *K*). Asn13–Tyr16 is located in the outer surface region to which the disordered N-terminal tail is connected. Ala139–Asp141, the loop region between helices α4 and α5, is located just beside the hydrophilic Asp channel along a threefold axis of the 23 symmetry described below. Ser22–Lys27, the N-terminal region of helix α1, is located between the two aforementioned regions showing structural differences. These differences suggest conformational flexibility within these regions.

3.2. The ferroxidase center

In the $F_{iron-soaked} - F_{native}$ difference Fourier map, where F_{native} and $F_{iron-soaked}$ are the structure amplitudes of the native and iron-soaked forms, respectively, at a wavelength of 1.0000 Å, high peaks of at least 8σ above the average were observed at the FOCs. High peaks of 35σ above the average were also observed at the FOCs in the phased Bijvoet difference map calculated using diffraction data collected at a wavelength of 1.7400 Å, where the imaginary part of the anomalous scattering f'' of the Fe atom is 3.9 electrons (Sasaki, 1989). In contrast, the heights of the peaks at the FOCs have much a lower value of approximately 4σ above the average in the phased Bijvoet difference map calculated using the diffraction data collected at a wavelength of 1.7500 Å, where f'' is approximately 0.47 electrons (Sasaki, 1989). These observations clearly indicate that iron ions are bound to the FOCs in the iron-soaked crystal. The average B factor of the 12 iron ions is 24.7 Å, with a standard deviation of 0.9 Å. The B factors of the iron ions are comparable to those of the protein atoms liganding to the iron ions, suggesting that all of the FOCs are fully occupied by iron ions. The iron ions are thought to be Fe^{II}, since the soaking with iron ions took place in the presence of the antioxidant ascorbic acid. The FOC is situated at the dimeric interface of two protomers and the iron ion is located between the acidic side chains of Asp78 and Glu82 of one protomer and the basic side chains of His51, Lys48 and His63 of the other protomer (Fig. 2*a*). The iron ion is coordinated by Asp78 $O^{\delta1}$ and $O^{\delta2}$ as a bidentate ligand, Glu83 $O^{\varepsilon2}$, His51 $N^{\varepsilon2}$ and two water molecules (waters 1 and 2) in a distorted octahedral geometry. The amino-acid residues liganding the iron ion are highly conserved in the DPS-like protein family (Haikarainen & Papageorgiou, 2010). The side chains of Lys48 and His43 are hydrogen-bonded to waters 1 and 2, respectively. The coordination distances of Asp78 $O^{\delta1}$, Asp78 $O^{\delta2}$, His51 $N^{\varepsilon2}$ and water 2 are 2.12–2.38 Å, whereas those of Glu82 $O^{\varepsilon2}$ and water 1 have slightly shorter values of 1.96 and 1.91 Å, respectively (Table 2). Glu82 $O^{\varepsilon2}$ and water 1 are coordinated to the iron ion from the direction perpendicular to the plane formed by Asp78 $O^{\delta1}$, Asp78 $O^{\delta2}$, His51 $N^{\varepsilon2}$ and water 2. Although the six-coordinated octahedral geometry of Fe^{II} at the FOC was also observed in the structures of the homologous *Halobacterium salinarum* DpsA at 2.2 Å resolution (PDB entry 1tkp; Zeth *et al.*, 2004) and *Deinococcus radiodurans* Dps2 at 2.1 Å resolution (PDB entry 2c26; Cuypers *et al.*, 2007), these shorter coordination distances were unnoticed, probably owing to the lower structural resolution, and are elucidated for the first time by the high-resolution crystal structure of iron-soaked SEp22. In contrast to the single iron ion bound to FOC in the SEp22 crystal structure, a μ-oxo-bridged di-iron, Fe^{III}–O–Fe^{III}, was observed at the FOC of the homologous

Bacillus brevis Dps (Ren *et al.*, 2003). The iron-soaked SEp22 structure may represent the state just after the first Fe^{II} ion to be oxidized binds to the FOC.

In the native SEp22 crystal no iron ion is bound to the FOC (Fig. 2*b*). Instead, a magnesium ion is coordinated by five water molecules and located near the FOC. The side chains of Asp78, Glu82 and Lys48 are hydrogen bonded to the water molecules coordinated to the magnesium ion. Of the residues at the FOC, Asp78 shows the largest conformational change upon iron ion binding. Although the side chain of Asp78 extends away from the iron-binding site in the native form, it flips with an ∼100° rotation around the χ_1 torsion angle toward the bound iron ion and coordinates to the ion in the iron-soaked form.

3.3. The hydrophilic channels and hydrophobic welds along the threefold axes

The assembly of the protomers in 23 symmetry generates eight threefold-related pores, which are classified into two distinct types based on the residues composing the pores: four Asp channels and four Ala welds. The Asp channels constitute the C-terminal region of helix $\alpha4$ (Leu136–Glu138), the loop region between helices $\alpha4$ and $\alpha5$ (Ala139–Glu142) and the N-terminal region of helix $\alpha5$ (Asp143–Thr149). The Asp channels are hourglass-shaped, with dimensions of ∼22 Å in length, 14 Å in diameter for the outer opening, 1.7 Å in diameter around the constriction at Asp146 and 12 Å in diameter for the inner opening. The constriction consists of three Asp146 residues whose side-chain carboxylate groups are arranged triangularly and oriented towards the inside of the dodecameric shell of SEp22; the distances between neighbouring $O^{\delta1}$ atoms of their side chains are approximately 4.3 Å (Fig. 2*c*). Magnesium ions are located in close proximity to the entrances of all of the Asp channels. The magnesium ions are octahedrally coordinated by six water molecules, three of which form hydrogen bonds to three Asp146 $O^{\delta1}$ atoms. The threefold axes of the octahedrally coordinated magnesium ions are almost coincident with the threefold axes at the Asp channels.

The Ala welds are formed by the N-terminal region of helix $\alpha1$ (Ala57–Glu64) and Glu167. They are also hourglass-shaped, with sizes of approximately 12 Å in length, 3.5 Å in diameter for the outer opening, 0.5 Å in diameter for the constriction around Ala61 and 2.5 Å in diameter for the inner opening. The Ala61 C^{β} atoms at the constriction point are closely packed around a threefold axis as shown in Fig. 2(*d*).

As the effective ionic radii of iron ions are 0.61 Å for Fe^{2+} and 0.55 Å for Fe^{3+} (Shannon, 1976), iron ions are thought to flow into the cavity of SEp22 through the Asp channel, the narrowest diameter of which is approximately 1.7 Å. The negatively charged Asp residues within the channel are suitable for the iron ion. When an iron ion, which is thought to be octahedrally coordinated by six water molecules in solution, passes through the Asp channel, the water molecules coordinating to the iron ion would initially form hydrogen bonds to Asp146 $O^{\delta1}$ as in the case of the hydrated magnesium ion shown in Fig. 2(*c*); Asp146 $O^{\delta1}$ may then replace the water molecules of the hydrated iron ion and coordinate directly to the ion.

In some Dps dodecamers it has been proposed that the hydrophobic pores along the threefold axis (the Ala weld in the case of SEp22) could represent auxiliary exits for the iron ions (Romao *et al.*, 2006; Franceschini *et al.*, 2006). The diameter of the pore at the Ala weld in SEp22 is much smaller than the size of iron ions and the conformational changes that would lead to a widening of the pore are impossible because Ala61 is involved in tight van der Waals contacts with the surrounding residues. These observations indicate that the Ala welds in SEp22 could not function as exit points for the iron ions.

References

Almiron, M., Link, A. J., Furlong, D. & Kolter, R. (1992). *Genes Dev.* **6**, 2646–2654.

Bearden, J. A. (1967). *Rev. Mod. Phys.* **39**, 78–124.

Collaborative Computational Project, Number 4 (1994). *Acta Cryst.* D**50**, 760–763.

Cuypers, M. G., Mitchell, E. P., Romao, C. V. & McSweeney, S. M. (2007). *J. Mol. Biol.* **371**, 787–799.

Dundas, J., Ouyang, Z., Tseng, J., Binkowski, A., Turpaz, Y. & Liang, J. (2006). *Nucleic Acids Res.* **34**, W116–W118.

Emsley, P. & Cowtan, K. (2004). *Acta Cryst.* D**60**, 2126–2132.

Franceschini, S., Ceci, P., Alaleona, F., Chiancone, E. & Ilari, A. (2006). *FEBS J.* **273**, 4913–4928.

Gasteiger, E., Hoogland, C., Gattiker, A., Duvaud, S., Wilkins, M. R., Appel, R. D. & Bairoch, A. (2005). *The Proteomics Protocols Handbook*, edited by J. M. Walker, pp. 571–607. Totowa: Humana Press.

Grant, R. A., Filman, D. J., Finkel, S. E., Kolter, R. & Hogle, J. M. (1998). *Nature Struct. Biol.* **5**, 294–303.

Haikarainen, T. & Papageorgiou, A. C. (2010). *Cell. Mol. Life Sci.* **67**, 341–351.

Imlay, J. A. (2003). *Annu. Rev. Microbiol.* **57**, 395–418.

Laskowski, R. A., MacArthur, M. W., Moss, D. S. & Thornton, J. M. (1993). *J. Appl. Cryst.* **26**, 283–291.

Lovell, S. C., Davis, I. W., Arendall, W. B. III, de Bakker, P. I., Word, J. M., Prisant, M. G., Richardson, J. S. & Richardson, D. C. (2003). *Proteins*, **50**, 437–450.

Maiti, R., Van Domselaar, G. H., Zhang, H. & Wishart, D. S. (2004). *Nucleic Acids Res.* **32**, W590–W594.

Murshudov, G. N., Vagin, A. A. & Dodson, E. J. (1997). *Acta Cryst.* D**53**, 240–255.

Nataro, J. P., Bopp, C. A., Fields, P. I., Kaper, J. B. & Strockbine, N. A. (2007). *Manual of Clinical Microbiology*, 9th ed., edited by P. R. Murray, Vol. 1, pp. 679–680. Washington: ASM Press.

Otwinowski, Z. & Minor, W. (1997). *Methods Enzymol.* **276**, 307–326.

Pettersen, E. F., Goddard, T. D., Huang, C. C., Couch, G. S., Greenblatt, D. M., Meng, E. C. & Ferrin, T. E. (2004). *J. Comput. Chem.* **25**, 1605–1612.

Poornam, G., Matsumoto, A., Ishida, H. & Hayward, S. (2009). *Proteins*, **76**, 2001–2021.

Ren, B., Tibbelin, G., Kajino, T., Asami, O. & Ladenstein, R. (2003). *J. Mol. Biol.* **329**, 467–477.

Romao, C. V., Mitchell, E. P. & McSweeney, S. (2006). *J. Biol. Inorg. Chem.* **11**, 891–902.

Roy, S., Gupta, S., Das, S., Sekar, K., Chatterji, D. & Vijayan, M. (2004). *J. Mol. Biol.* **339**, 1103–1113.

Roy, S., Saraswathi, R., Gupta, S., Sekar, K., Chatterji, D. & Vijayan, M. (2007). *J. Mol. Biol.* **370**, 752–767.

Sasaki, S. (1989). *KEK Report 88–14*, p. 53. KEK, Photon Factory, Tsukuba, Japan.

Shannon, R. D. (1976). *Acta Cryst.* A**32**, 751–767.

Stillman, T. J., Upadhyay, M., Norte, V. A., Sedelnikova, S. E., Carradus, M., Tzokov, S., Bullough, P. A., Shearman, C. A., Gasson, M. J., Williams, C. H., Artymiuk, P. J. & Green, J. (2005). *Mol. Microbiol.* **57**, 1101–1112.

Terai, S., Yamasaki, M., Igimi, S. & Amano, F. (2005). *Biosci. Microflora*, **24**, 113–118.

Terai, S., Yasuda, M. & Amano, F. (2006). *Microbes Environ.* **21**, 36–43.

Vaguine, A. A., Richelle, J. & Wodak, S. J. (1999). *Acta Cryst.* D**55**, 191–205.

Zeth, K., Offermann, S., Essen, L.-O. & Oesterhelt, D. (2004). *Proc. Natl Acad. Sci. USA*, **101**, 13780–13785.

Zhao, G., Ceci, P., Ilari, A., Giangiacomo, L., Laue, T. M., Chiancone, E. & Chasteen, N. D. (2002). *J. Biol. Chem.* **277**, 27689–27696.